

Vortex-bright solitons in a spin-orbit coupled spin-1 condensate

Sandeep Gautam* and S. K. Adhikari†

*Instituto de Física Teórica,
Universidade Estadual Paulista - UNESP,
01.140-070 São Paulo, São Paulo, Brazil*

(Dated: June 20, 2018)

We study the vortex-bright solitons in a quasi-two-dimensional spin-orbit-coupled (SO-coupled) hyperfine spin-1 three-component Bose-Einstein condensate (BEC) using variational method and numerical solution of a mean-field model. The ground state of these vortex-bright solitons is radially symmetric for weak ferromagnetic and polar interactions. For a sufficiently strong ferromagnetic interaction, we observe the emergence of an asymmetric vortex-bright soliton as the ground state. We also numerically investigate stable moving solitons and binary collision between them. The present mean-field model is not Galilean invariant, and we use a Galilean-transformed model for generating the moving solitons. At low velocities, the head-on collision between two *in-phase* solitons results either in collapse or fusion of the soliton pair. On the other hand, in head-on collision, the two *out-of-phase* solitons strongly repel each other and trace back their trajectories before the actual collision. At low velocities, in a collision with an impact parameter, the *out-of-phase* solitons get deflected from their original trajectory like two rigid classical disks. These *out-of-phase solitons* behave like classical disks, and their collision dynamics is governed by classical laws of motion. However, at large velocities two SO-coupled spinor solitons, irrespective of phase difference, can pass through each other in a head-on collision like two quantum solitons.

PACS numbers: 03.75.Mn, 03.75.Hh, 67.85.Bc, 67.85.Fg

I. INTRODUCTION

A self-reinforcing solitary wave which preserves its shape while traversing at a constant speed is known as a bright soliton. The origin of the bright solitons is due to a cancellation of the effects produced by non-linear and dispersive terms in the Hamiltonian. Solitons have been studied in a wide range of systems ranging from water waves, non-linear optics [1], ultracold quantum gases including spinor Bose-Einstein condensates (BECs) [2–6], etc. In this paper, we study the two-dimensional (2D) vortex-bright solitons in spin-orbit (SO) coupled three-component spin-1 spinor Bose-Einstein condensates. The SO coupling is the coupling between the spin of the atom and its center of mass motion. In neutral atoms, the SO coupling is absent [7]. Nevertheless, neutral atoms can be subjected to the SO coupling by creating a non-Abelian gauge potential by suitably modifying the atom-light interaction [8]. The SO coupling with equal strengths of Rashba [9] and Dresselhaus [10] terms was first engineered in a landmark experiment with a BEC of ^{87}Rb by dressing two of its internal spin states from within the ground electronic manifold ($5S_{1/2}, F = 1$) with a pair of lasers [11]. In recent years, a variety of experimental studies have been done on SO-coupled Bose-Einstein condensates [12]. Solitonic structures have been theoretically investigated in SO-coupled quasi-one-dimensional (quasi-1D) [13] and quasi-2D pseudospin-1/2 condensates [14, 15]. Bright solitons have also been theoretically stud-

ied in SO-coupled quasi-1D spin-1 [16, 17] and spin-2 condensates [18].

In this paper, we study the stable stationary and moving vortex-bright solitons in a quasi-2D [19] SO-coupled spin-1 condensate using the mean-field Gross-Pitaevskii (GP) equations [20]. We observe that for small strengths of SO coupling which we employ in the paper, the ground state vortex-bright soliton of an SO-coupled polar and weakly-ferromagnetic spin-1 condensate is an axisymmetric vortex-bright soliton of type $(-1, 0, +1)$ with zero magnetization, where the numbers in the parenthesis are the phase-winding numbers (angular momenta) [21] associated with the spin components $m_f = +1, 0, 1$. An anti-vortex in component $m_f = +1$ is associated with an overlapping vortex of opposite circulation in $m_f = -1$ component. Besides this, we have also identified a stationary excited axisymmetric vortex-bright soliton of type $(0, +1, +2)$. The spin texture of this excited state vortex-bright soliton shows that it is a *coreless Anderson-Toulouse* vortex [21]. For condensates with stronger ferromagnetic interaction, the ground state is an asymmetric vortex-bright soliton with an anti-vortex of unit charge in the spin component $m_f = +1$ associated with a vortex of opposite circulation in the $m_f = -1$ component. In this case the vortex and anti-vortex are separated from each other, and the separation can occur along any arbitrary direction, which will get spontaneously chosen in an experiment, in two-dimensional plane. However, the condensate collapses for very strong ferromagnetic interaction and no vortex-bright soliton can be formed.

The 2D vortex-bright solitons were first suggested and studied in the pseudospin-1/2 two-component spin-1 BEC [15], which is an approximation over the present three-component model of spin-1 BEC. In general, the

*sandeepgautam24@gmail.com

†adhikari44@yahoo.com, URL <http://www.ift.unesp.br/users/adhikari>

implementation of SO interaction in the three-component spin-1 BEC is more complicated than the same in the two-component pseudospin-1/2 BEC from both theoretical [22] and experimental [23] point of view. The present study goes beyond that previous investigation [15]. It provides a more intuitive understanding of the role of SO coupling in generating the solitons, viz. Figs. 1(a)-(b), in addition to a critical study of statics and interaction dynamics of the 2D solitons. Although these solitons behave as true solitons in frontal collision at high velocities, at low velocities, depending on the relative phase, they may repel and bounce back like in the collision of two rigid elastic disks or may transfer all atoms to one soliton to form a soliton molecule. Only the collision of two 1D analytic solitons is truly elastic at all velocities.

Besides stationary vortex-bright solitons, we have also investigated the stable moving vortex-bright soliton of the SO-coupled spin-1 condensate. As the present mean-field model does not possess Galilean invariance, the moving solitons are calculated with the Galilean-transformed model [13, 15–17]. We find that the structure of the moving vortex-bright soliton is a function of both the magnitude and the direction of velocity, which can result in different density distributions for vortex-bright solitons moving along different directions. At low velocities, the collision of two vortex-bright solitons with a phase difference of π is elastic. The two solitons repel and avoid each other and rebound from the center of collision without ever forming an overlapped profile. The collision dynamics is demonstrated to obey classical laws of motion. If the same initial guess is used for the right and the left moving solitons in the numerical simulation of the stationary state, the solitons acquire a phase difference of π . If this phase difference is removed before the numerical simulation of the colliding solitons, then after the collision between the two slow moving vortex-bright solitons, all the atoms end up being captured by one of the solitons. Similarly, in the collision of two normal BEC solitons at sufficiently low velocities, the two colliding solitons lose their identity and form a stable overlapping profile called a soliton molecule [24, 25]. At large velocities, the two vortex-bright solitons undergo quasi-elastic collision with the two solitons crossing each other irrespective of the phase difference.

The paper is organized as follows. In Sec. II A, we describe the mean-field coupled Gross-Pitaevskii (GP) equations with Rashba SO coupling used to study the vortex-bright solitons in a spin-1 condensate. This is followed by a variational analysis of the stationary axisymmetric vortex-bright solitons in Sec. II B. In Sec. III, we provide the details of the numerical method used to solve the coupled GP equations with SO coupling. We discuss the numerical results for axisymmetric vortex-bright solitons in Sec. IV A, asymmetric solitons in Sec. IV B, stability of the solitons in Sec. IV C, and moving solitons and collisions between solitons in Sec. IV D. Finally, in Sec. V, we give a summary of our findings.

II. SPIN-ORBIT COUPLED BEC VORTEX-BRIGHT SOLITON

A. Mean-field equations

For the study of a quasi-2D vortex-bright soliton, we consider a spin-1 spinor BEC under a harmonic trap $m\omega_z^2 z^2/2$ in the z direction and free in the $x - y$ plane. After integrating out the z coordinate, the single particle Hamiltonian of the condensate with Rashba [9] SO coupling in such a quasi-2D trap is [26]

$$H_0 = \frac{p_x^2 + p_y^2}{2m} + \gamma p_x \Sigma_x + \gamma p_y \Sigma_y, \quad (1)$$

where $p_x = -i\hbar\partial/\partial x$ and $p_y = -i\hbar\partial/\partial y$ are the momentum operators along x and y axes, respectively, and Σ_x and Σ_y are the irreducible representations of the x and y components of the spin matrix, respectively,

$$\Sigma_x = \frac{1}{\sqrt{2}} \begin{pmatrix} 0 & 1 & 0 \\ 1 & 0 & 1 \\ 0 & 1 & 0 \end{pmatrix}, \quad \Sigma_y = \frac{1}{\sqrt{2}i} \begin{pmatrix} 0 & 1 & 0 \\ -1 & 0 & 1 \\ 0 & -1 & 0 \end{pmatrix}, \quad (2)$$

and γ is the strength of SO coupling. In the mean-field approximation, the SO-coupled quasi-2D spin-1 BEC is described by the following set of three coupled two-dimensional GP equations, written here in dimensionless form, for different spin components $m_f = \pm 1, 0$ [20, 27]

$$i \frac{\partial \psi_{\pm 1}(\mathbf{r})}{\partial t} = \mathcal{H} \psi_{\pm 1}(\mathbf{r}) \pm c_1 F_z \psi_{\pm 1}(\mathbf{r}) + \frac{c_1}{\sqrt{2}} F_{\mp} \psi_0(\mathbf{r}) - \frac{i\gamma}{\sqrt{2}} \left(\frac{\partial \psi_0}{\partial x} \mp i \frac{\partial \psi_0}{\partial y} \right), \quad (3)$$

$$i \frac{\partial \psi_0(\mathbf{r})}{\partial t} = \mathcal{H} \psi_0(\mathbf{r}) + \frac{c_1}{\sqrt{2}} [F_- \psi_{-1}(\mathbf{r}) + F_+ \psi_{+1}(\mathbf{r})] - \frac{i\gamma}{\sqrt{2}} \left(\frac{\partial \psi_1}{\partial x} + i \frac{\partial \psi_1}{\partial y} + \frac{\partial \psi_{-1}}{\partial x} - i \frac{\partial \psi_{-1}}{\partial y} \right), \quad (4)$$

where $\mathbf{F} \equiv \{F_x, F_y, F_z\}$ is a vector whose three components are the expectation values of the three spin-operators over the multicomponent wavefunction, and is called the spin-expectation value [27]. Also,

$$F_{\pm} \equiv F_x \pm iF_y = \sqrt{2}[\psi_{\pm 1}^*(\mathbf{r})\psi_0(\mathbf{r}) + \psi_0^*(\mathbf{r})\psi_{\mp 1}(\mathbf{r})], \quad (5)$$

$$F_z = \rho_{+1}(\mathbf{r}) - \rho_{-1}(\mathbf{r}), \quad \mathcal{H} = -\frac{\nabla^2}{2} + c_0 \rho, \quad (6)$$

$$c_0 = \frac{2N\sqrt{2\pi}(a_0 + 2a_2)}{3l_0}, \quad c_1 = \frac{2N\sqrt{2\pi}(a_2 - a_0)}{3l_0}, \quad (7)$$

$$\nabla^2 = \frac{\partial^2}{\partial x^2} + \frac{\partial^2}{\partial y^2}, \quad \mathbf{r} \equiv \{x, y\}, \quad (8)$$

where $\rho_j = |\psi_j(\mathbf{r})|^2$ with $j = \pm 1, 0$ are the component densities, $\rho = \sum_j \rho_j$ is the total density, a_0 and a_2 are the s -wave scattering lengths in the total spin 0 and 2 channels, respectively, and asterisk denotes complex conjugate. The normalization condition satisfied

by the component wavefunctions ψ_j is $\int \sum_j \rho_j d\mathbf{r} = 1$. All quantities in Eqs. (3)-(8) are dimensionless. This is achieved by writing length, density, and energy in units of l_0 ($= \sqrt{\hbar/(M\omega_z)}$), l_0^{-2} , and $\hbar\omega_z$, respectively. The energy of the system in dimensionless unit is

$$E = \int_{-\infty}^{\infty} d\mathbf{r} \left\{ \frac{1}{2} \left(\sum_{j=-1}^1 |\nabla\psi_j|^2 + c_0\rho^2 + c_1|\mathbf{F}|^2 \right) - \frac{i\gamma}{\sqrt{2}}\psi_0^* \left(\frac{\partial\psi_1}{\partial x} + \frac{\partial\psi_{-1}}{\partial x} \right) + \frac{\gamma}{\sqrt{2}}\psi_0^* \left(\frac{\partial\psi_1}{\partial y} - \frac{\partial\psi_{-1}}{\partial y} \right) - \frac{i\gamma}{\sqrt{2}}(\psi_1^* + \psi_{-1}^*) \frac{\partial\psi_0}{\partial x} - \frac{\gamma}{\sqrt{2}}(\psi_1^* - \psi_{-1}^*) \frac{\partial\psi_0}{\partial y} \right\}. \quad (9)$$

In plane polar coordinates, $\mathbf{r} = (r, \phi)$, Eqs. (3)-(4) are

$$i \frac{\partial\psi_{\pm 1}(r, \phi)}{\partial t} = \mathcal{H}(r, \phi)\psi_{\pm 1}(r, \phi) \pm c_1 F_z \psi_{\pm 1}(r, \phi) + \frac{c_1}{\sqrt{2}} F_{\mp} \psi_0(r, \phi) - \frac{i\gamma e^{\mp i\phi}}{\sqrt{2}} \left(\frac{\partial\psi_0}{\partial r} \mp i \frac{\partial\psi_0}{r\partial\phi} \right), \quad (10)$$

$$i \frac{\partial\psi_0(r, \phi)}{\partial t} = \mathcal{H}(r, \phi)\psi_0(r, \phi) + \frac{c_1}{\sqrt{2}} [F_- \psi_{-1}(r, \phi) + F_+ \psi_{+1}(r, \phi)] - \frac{i\gamma}{\sqrt{2}} \left[e^{i\phi} \left(\frac{\partial\psi_1}{\partial r} + i \frac{\partial\psi_1}{r\partial\phi} \right) + e^{-i\phi} \left(\frac{\partial\psi_{-1}}{\partial r} - i \frac{\partial\psi_{-1}}{r\partial\phi} \right) \right]. \quad (11)$$

The coupled Eqs. (10)-(11) in polar coordinates are instructive to understand the underlying symmetries of the system.

B. Vortex-bright soliton

This study revealed two types of stationary quasi-2D low-energy axisymmetric vortex-bright solitons in an SO-coupled spin-1 BEC for an attractive (negative) c_0 and for $c_1 \geq c_1^{(1)}$ corresponding to polar ($c_1 > 0$) and weak ferromagnetic ($0 > c_1 \geq c_1^{(1)}$) domains; at higher energies there could be other states. As c_1 is decreased further deep into ferromagnetic ($c_1 < c_1^{(1)}$) domain, the axisymmetric vortex-bright solitons are no longer the lowest-energy states. For $c_1^{(1)} > c_1 > c_1^{(2)}$, a new type of asymmetric soliton emerges with an energy lower than the axisymmetric soliton(s), which become excited states. Eventually, all types of states collapse for $c_1 < c_1^{(2)}$ because of an excess of attraction. The numerical values of c_1 , e.g. $c_1^{(1)}$ and $c_1^{(2)}$, for the appearance of an asymmetric soliton for $c_1 \leq c_1^{(1)}$, and finally, its collapse for $c_1 \leq c_1^{(2)}$ depend on c_0 and γ . Using the phase-winding numbers (angular momentum) of the three-component wavefunction to denote a vortex [21], the axisymmetric vortex-bright solitons are classified as $(-1, 0, +1)$ and

$(0, +1, +2) \equiv (-2, -1, 0)$ solitons, where the numbers in the parenthesis are the phase-winding numbers of ψ_{+1} , ψ_0 and ψ_{-1} , respectively. Here the \pm signs in the winding number denote a vortex and an anti-vortex rotating in opposite directions, respectively. For example, the soliton $(-1, 0, +1)$ denotes a state of angular momentum ∓ 1 in components $\psi_{\pm 1}$ and angular momentum 0 in component ψ_0 . Here, the cores of the vortices in $m_f = \pm 1$ components are occupied by the polar ($m_f = 0$) component, and thus these solitons can be termed *polar-core* vortex-bright solitons. There are no stable stationary axisymmetric solitons of type $(0, 0, 0)$ without any angular momentum in all components. The details of a $(-1, 0, +1)$ vortex-bright soliton – energy and density – are independent of the value of c_1 – positive or negative. This is due to the fact that for the stable minimum energy solitons of this type spin density vector \mathbf{F} is uniformly zero. However, the same of a $(0, +1, +2)$ vortex-bright soliton and an asymmetric vortex-bright soliton are dependent on c_1 . We will use a variational method to analytically study the axisymmetric vortex-bright solitons below.

Our numerical studies show that the longitudinal magnetization $\mathcal{M} = \int \{\rho_{+1}(\mathbf{r}) - \rho_{-1}(\mathbf{r})\} d\mathbf{r}$ is zero for the $(-1, 0, +1)$ solitons; whereas it can be non-zero for the $(0, +1, +2)$ solitons. This guides our choices of simple variational *ansatz* to model the vortex-bright solitons. The $(-1, 0, +1)$ vortex-bright soliton with zero magnetization \mathcal{M} can be analyzed using the following variational *ansatz*

$$\psi_{\pm 1} = \frac{A_1 r}{\sigma_1^2} \exp\left(-\frac{r^2}{2\sigma_1^2} \mp i\phi\right), \quad (12)$$

$$\psi_0 = i \frac{A_2}{\sigma_2} \exp\left(-\frac{r^2}{2\sigma_2^2}\right), \quad (13)$$

where $r = \sqrt{x^2 + y^2}$ and $\phi = \tan^{-1}(y/x)$ are the radial and azimuthal coordinates, A_i, σ_i are the variational parameters, which denote the amplitude and the width of the component wavefunctions, respectively. The condition of zero magnetization fixes the amplitudes of components $\psi_{\pm 1}$ to be equal. The equal and opposite phases ($\mp\phi$) of these components guarantee their opposite directions of rotation with unit angular momentum – vortex and anti-vortex. Only three of the variational parameters are independent of each other as the fourth, say A_2 , is fixed by the normalization ($= 1$). The variational energy of the soliton, obtained by substituting Eqs. (12) and (13) in Eq. (9), is

$$E = \frac{\pi}{2} \left[\left\{ \frac{A_2^2}{\sigma_2^2} + \frac{4A_1^2}{\sigma_1^2} - \frac{16\sqrt{2}A_1A_2\gamma\sigma_1^2\sigma_2}{(\sigma_1^2 + \sigma_2^2)^2} \right\} + c_0 \left\{ \frac{A_1^4}{\sigma_1^2} + \frac{4A_1^2A_2^2\sigma_2^2}{(\sigma_1^2 + \sigma_2^2)^2} + \frac{A_2^4}{2\sigma_2^2} \right\} \right], \quad (14)$$

where A_2 is determined by the normalization constraint:

$$A_2 = \frac{\sqrt{1 - 2\pi A_1^2}}{\sqrt{\pi}}. \quad (15)$$

As mentioned earlier, in this case $|\mathbf{F}|^2 = 0$; consequently, variational energy (14) is independent of c_1 . Energy (14) can be minimized with respect to the variational parameters A_i and σ_i , with Eq. (15) acting as a constraint, to determine A_i and σ_i . The numerical result for the component wave functions of a stationary $(-1, 0, +1)$ vortex-bright soliton is obtained by an imaginary-time simulation of Eqs. (3) and (4) with an initial guess of component wave functions (12) and (13). In case of axisymmetric $(-1, 0, +1)$ ground state solutions, ansatz (12) and (13) ensure faster convergence of the numerical results as compared to Gaussian initial guess for the three-component wavefunction, which also lead to the same final converged solutions.

Next we consider the axisymmetric $(0, +1, +2)$ vortex-bright soliton, which has higher energy than an axisymmetric $(-1, 0, +1)$ vortex-bright soliton with the same parameters c_0, c_1 , and γ . For a variational study of the $(0, +1, +2)$ vortex-bright soliton, we adopt the following variational *ansatz*

$$\psi_{+1} = i \frac{A_1}{\sigma_1} \exp\left(-\frac{r^2}{2\sigma_1^2}\right) \quad (16)$$

$$\psi_0 = \frac{A_2}{\sigma_2} r \exp\left(-\frac{r^2}{2\sigma_2^2} + i\phi\right) \quad (17)$$

$$\psi_{-1} = -i \frac{A_3}{\sigma_3} r^2 \exp\left(-\frac{r^2}{2\sigma_3^2} + i2\phi\right), \quad (18)$$

where A_i and σ_i are the variational parameters for the amplitude and the width of the component wave functions. The phases $0, \phi$, and 2ϕ of the components ψ_{+1}, ψ_0 , and ψ_{-1} , respectively, ensure their angular momenta as $(0, +1, +2)$. In the case of a $(-1, 0, +1)$ vortex-bright soliton, the zero magnetization condition ($\mathcal{M} = 0$) fixes the amplitudes of the wave function components $\psi_{\pm 1}$ to be equal. Our numerical simulations confirm that this is not the case for a stable $(0, +1, +2)$ vortex-bright soliton where, in general, $\mathcal{M} \neq 0$. Hence, a fixed norm ($=1$) is the only constraint, which reduces the number of independent variational parameters ($=6$) by one. Using Eqs. (16)-(18), the energy (9) of the soliton can be written as

$$\begin{aligned} E = & \frac{1}{8}\pi \left[4 \left\{ \frac{A_1^2}{\sigma_1^2} + 2 \frac{A_2^2}{\sigma_2^2} - \frac{8\sqrt{2}A_1A_2\gamma\sigma_1\sigma_2^2}{(\sigma_1^2 + \sigma_2^2)^2} + 6 \frac{A_3^2}{\sigma_3^2} - \frac{32\sqrt{2}A_2A_3\gamma\sigma_2^2\sigma_3^3}{(\sigma_2^2 + \sigma_3^2)^3} \right\} \right. \\ & + c_0 \left\{ 2 \frac{A_1^4}{\sigma_1^2} + 3 \frac{A_3^4}{\sigma_3^2} + \frac{48A_2^2A_3^2\sigma_2^4\sigma_3^2}{(\sigma_2^2 + \sigma_3^2)^4} + A_1^2 \left(\frac{8A_2^2\sigma_1^2}{(\sigma_1^2 + \sigma_2^2)^2} + \frac{16A_3^2\sigma_1^4}{(\sigma_1^2 + \sigma_3^2)^3} \right) + \frac{A_2^4}{\sigma_2^2} \right\} \\ & \left. + c_1 \left\{ 2 \frac{A_1^4}{\sigma_1^2} + 3 \frac{A_3^4}{\sigma_3^2} + \frac{48A_2^2A_3^2\sigma_2^4\sigma_3^2}{(\sigma_2^2 + \sigma_3^2)^4} + A_1^2 \left(\frac{8A_2^2\sigma_1^2}{(\sigma_1^2 + \sigma_2^2)^2} - \frac{16A_3^2\sigma_1^4}{(\sigma_1^2 + \sigma_3^2)^3} \right) + \frac{256A_1A_2^2A_3\sigma_1^5\sigma_2^2\sigma_3^3}{(\sigma_2^2\sigma_3^2 + 2\sigma_1^2\sigma_3^2 + \sigma_1^2\sigma_2^2)^3} \right\} \right]. \quad (19) \end{aligned}$$

The condition of fixed norm ($= 1$) leads to one constraint relating the variational parameters A_i and σ_i :

$$\pi(A_1^2 + A_2^2 + 2A_3^2) = 1. \quad (20)$$

Minimizing energy (19) with respect to the variational parameters A_i and σ_i under the constraint (20), one can determine the variational parameters.

For a $(-2, -1, 0)$ vortex-bright soliton which is degenerate with a $(0, +1, +2)$ soliton, the appropriate variational ansatz can be obtained from Eqs. (16)-(18) by transformations $\psi_{m_f}(r, \phi) \rightarrow \psi_{-m_f}(r, -\phi)$ or $\psi_{m_f}(x, y) \rightarrow \psi_{-m_f}(x, -y)$. The degeneracy of these states is due to underlying symmetry of Eqs. (3)-(4), which remain invariant under the transformation $y \rightarrow -y$ and $\psi_{m_f}(x, y) \rightarrow \psi_{-m_f}(x, -y)$. Under this transforma-

tion, a $(-1, 0, +1)$ vortex-bright soliton transforms into itself as can be confirmed from the variational ansatz (12)-(13); hence there is no degenerate counterpart for a $(-1, 0, +1)$ vortex-bright soliton. Equations (16)-(18) are invariant under simultaneous transformations of $\gamma \rightarrow -\gamma$ and $\psi_0 \rightarrow \psi_0 e^{i\pi}$ (while keeping $\psi_{\pm 1}$ unchanged). It implies that for negative γ , the vortex-bright solitons are fundamentally identical to those for positive γ except for a phase difference of π in their $m_f = 0$ components.

III. NUMERICAL PROCEDURE

The coupled equations (3)-(4) can be solved by time-splitting Fourier Pseudo-spectral method [28] and time-

splitting Crank-Nicolson method [29–31]. Here, we extend the Fourier Pseudo-spectral method to the coupled GP equations with SO coupling terms and use the same to solve Eqs. (3)-(4). The coupled set of GP equations (3)-(4) can be represented in a simplified form as

$$\frac{i\partial\Psi}{\partial t} = (H_1 + H_2 + H_3)\Psi, \quad (21)$$

where $\Psi = (\psi_{+1}, \psi_0, \psi_{-1})^T$ with T denoting the transpose, H_1 , H_2 and H_3 are 3×3 matrix operators defined as

$$H_1 = \begin{pmatrix} \mathcal{H} + c_1(\rho_0 + \rho_-) & 0 & 0 \\ 0 & \mathcal{H} + c_1\rho_+ & 0 \\ 0 & 0 & \mathcal{H} + c_1(\rho_0 - \rho_-) \end{pmatrix}, \quad (22)$$

$$H_2 = \begin{pmatrix} 0 & c_1\psi_0\psi_{-1}^* & 0 \\ c_1\psi_0^*\psi_{-1} & 0 & \psi_0^*\psi_{+1} \\ 0 & c_1\psi_0\psi_{+1}^* & 0 \end{pmatrix}, \quad (23)$$

$$H_3 = -i\frac{\gamma}{\sqrt{2}} \begin{pmatrix} 0 & \partial_- & 0 \\ \partial_+ & 0 & \partial_- \\ 0 & \partial_+ & 0 \end{pmatrix}, \quad (24)$$

where

$$\rho_{\pm} = \rho_{+1} \pm \rho_{-1}, \quad \partial_{\pm} = \left(\frac{\partial}{\partial x} \pm i \frac{\partial}{\partial y} \right) \quad (25)$$

Now, the lowest order time-splitting involves solving the following equations successively

$$\frac{i\partial\Psi}{\partial t} = H_1\Psi, \quad (26)$$

$$\frac{i\partial\Psi}{\partial t} = H_2\Psi, \quad (27)$$

$$\frac{i\partial\Psi}{\partial t} = H_3\Psi. \quad (28)$$

Eq. (26) can be numerically solved using Fourier Pseudo-spectral method [29] which we employ in this paper or semi-implicit Crank-Nicolson method [31] and involves additional time-splitting of H_1 into its spatial derivative and non-derivative parts. The numerical solutions of Eq. (27) have been discussed in Refs. [29, 32]. We use Fourier Pseudo-spectral method to accurately solve Eq. (28). In Fourier space, Eq. (28) is

$$\frac{i\partial\tilde{\Psi}}{\partial t} = \tilde{H}_3\tilde{\Psi}, \quad (29)$$

where tilde indicates that the quantity has been Fourier transformed. Hamiltonian H_3 in Fourier space is

$$\tilde{H}_3 = -i\frac{\gamma}{\sqrt{2}} \begin{pmatrix} 0 & ik_x + k_y & 0 \\ ik_x - k_y & 0 & ik_x + k_y \\ 0 & ik_x - k_y & 0 \end{pmatrix} \quad (30)$$

The solution of Eq. (29) is

$$\tilde{\Psi}(t + dt) = e^{-i\tilde{H}_3 dt} \tilde{\Psi}(t) = e^{-i\hat{O}} \tilde{\Psi}(t), \quad (31)$$

$$= \left(I + \frac{\cos\Omega - 1}{\Omega^2} \hat{O}^2 - i \frac{\sin\Omega}{\Omega} \hat{O} \right) \tilde{\Psi}(t), \quad (32)$$

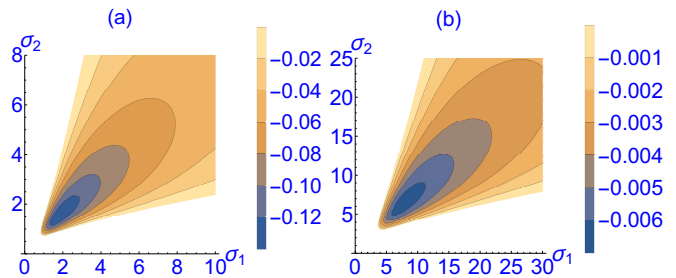


FIG. 1: (Color online) Two-dimensional contour plot of energy E of Eq. (14) as a function of widths σ_1 and σ_2 for (a) $c_0 = -4, \gamma = 0.5$ and (b) $c_0 = -5, \gamma = 0.1$. The actual values of A_1 and A_2 corresponding to the energy minima in these two cases have been used in Eq. (14) to prepare these plots.

where $\Omega = \sqrt{|A|^2 + |B|^2}$, where $A = -i\frac{\gamma}{\sqrt{2}}(ik_x + k_y) dt$ and $B = -i\frac{\gamma}{\sqrt{2}}(ik_x - k_y) dt$, and \hat{O} is defined as

$$\hat{O} = \begin{pmatrix} 0 & A & 0 \\ A^* & 0 & B^* \\ 0 & B & 0 \end{pmatrix}. \quad (33)$$

The wavefunction in Eq. (32) is in Fourier space and can be inverse Fourier transformed to obtain the solution in configuration space. In this study, in space and time discretizations, we use space and time steps of 0.1 and 0.005, respectively, in imaginary-time simulation, whereas in real-time simulation these are, respectively, 0.1 and 0.0005.

IV. NUMERICAL RESULTS

How the SO coupling creates a stable 2D soliton is explicit in the expression for energy (14). A stable bound soliton corresponds to a global minimum of the variational energy. In fact, for SO coupling $\gamma = 0$, this energy expression is positive and tends to zero as $\sigma_1, \sigma_2 \rightarrow \infty$ and does not have any minimum for $c_0 \geq -7$, beyond which $E \rightarrow -\infty$ as $\sigma_1, \sigma_2 \rightarrow 0$ and the system collapses. The contribution of the SO coupling to energy E of Eq. (14) is always negative in the form of a shallow well in the $\sigma_1 - \sigma_2$ plane. Hence by choosing $c_0 > -7$ (collapse-free region) and an adequate value of SO coupling γ , one can have a global minimum at negative energy in the energy expression (14) as a function of σ_1 and σ_2 corresponding to a stable 2D soliton. To illustrate how the SO coupling leads to a energy minimum we consider two examples: (a) $c_0 = -4, \gamma = -0.5$ and (b) $c_0 = -5, \gamma = -0.1$. In these two cases there is a energy minimum (a) $E_{\min} = -0.1441, \sigma_1 = 2.00, \sigma_2 = 1.588, A_1 = 0.2424$ and (b) $E_{\min} = -0.00668, \sigma_1 = 8.177, \sigma_2 = 6.587, A_1 = 0.221$. How the energy varies as a function of widths σ_1 and σ_2 for given amplitudes A_1 and A_2 can be seen in contour plots of energy as a function of the widths with the given amplitudes. These plots are shown in Figs. 1(a) and (b)

in these two cases explicitly showing the global minima of energy at negative energies. Outside the shaded areas in these plots, the energy function is zero or positive. The same thing also happens in the three-component energy function (19), which, however, is difficult to illustrate graphically.

A. Axisymmetric vortex-bright soliton

The numerical and analytic variational results for radial density $\rho(r)$ versus r for an axisymmetric $(-1, 0, +1)$ vortex-bright soliton for (a) $c_0 = -4, c_1 \geq -0.57$, and $\gamma = 0.5$ and for (b) $c_0 = -5, c_1 \geq -0.5$, and $\gamma = 0.1$ are shown in Figs. 2(a) and (b), respectively. The numerical result is obtained by an imaginary-time simulation of Eqs. (3) and (4) with the initial guess of component wave functions (12)-(13). The numerical and analytic variational results for radial density $\rho(r)$ versus r for the axisymmetric $(0, +1, +2)$ vortex-bright solitons for the same c_0, γ and $c_1 = -0.25$ are shown in Figs. 2(c) and (d). The numerical result in this case is obtained by an imaginary-time simulation of Eqs. (3) and (4) with the initial guess of component wave functions (16)-(18). The wave function components ψ_{+1}, ψ_0 , and ψ_{-1} in Figs. 2(a) and (b) carry angular momenta $-1, 0$ and $+1$ respectively, whereas in Figs. 2(c) and (d), they carry angular momenta $0, +1$ and $+2$. The $(-1, 0, +1)$ states of Fig. 2(a) and (b) are the ground states of the system, whereas the $(0, +1, +2)$ states of Fig. 2(c) and (d) are excited states. For $c_0 = -4, \gamma = 0.5$, viz. Figs. 2(a) and (c), the axisymmetric $(-1, 0, +1)$ vortex-bright soliton is the ground state for $c_1 \geq c_1^{(1)} = -0.57$ and for $c_0 = -5, \gamma = 0.1$, viz. Figs. 2(b) and (d), the axisymmetric $(-1, 0, +1)$ vortex-bright soliton is the ground state for $c_1 \geq c_1^{(1)} = -0.5$.

To describe the spatial orientation of the local magnetization vector in a spinor vortex BEC it is convenient to define a local magnetization vector \mathbf{l} , which points in the direction of spin, as the cross product of two vectors \mathbf{m} and \mathbf{n} [21]

$$\mathbf{l} = \mathbf{m} \times \mathbf{n}, \quad (34)$$

where $\mathbf{m} \equiv (m_x, m_y, m_z) = \text{Re}(\psi_x, \psi_y, \psi_z)$ and $\mathbf{n} \equiv (n_x, n_y, n_z) = \text{Im}(\psi_x, \psi_y, \psi_z)$, and

$$\psi_x = \frac{-\psi_{+1} + \psi_{-1}}{\sqrt{2}}, \quad (35)$$

$$\psi_y = \frac{-i(\psi_{+1} + \psi_{-1})}{\sqrt{2}}, \quad (36)$$

$$\psi_z = \psi_0, \quad (37)$$

where Re and Im stand for real and imaginary parts, respectively, ψ_x, ψ_y, ψ_z are the components of the order parameter in Cartesian basis [27]. An axisymmetric $(0, +1, +2)$ vortex can have two distinct spin textures

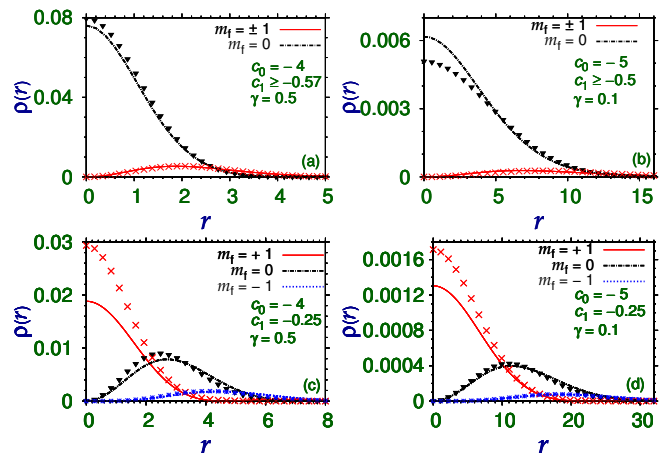


FIG. 2: (Color online) Numerical (line) and variational (chain of symbols) results for radial density $\rho(r)$ versus r of the components in an axisymmetric $(-1, 0, +1)$ vortex-bright soliton for (a) $c_0 = -4, c_1 \geq -0.57$, and $\gamma = 0.5$ and for (b) $c_0 = -5, c_1 \geq -0.5$, and $\gamma = 0.5$. The same in an axisymmetric $(0, +1, +2)$ vortex-bright soliton for (c) $c_0 = -4, c_1 = -0.25$, and $\gamma = 0.5$ and for (d) $c_0 = -5, c_1 = -0.25$, and $\gamma = 0.5$. All quantities in this and following figures are dimensionless.

[21] which are the spatial distribution of the local magnetization vector. For the $(0, +1, +2)$ vortex, the unit vector $\hat{\mathbf{l}} = \hat{z} \cos \beta(r) + \sin \beta(r)(\hat{x} \cos \phi + \hat{y} \sin \phi)$, here ϕ is the azimuthal angle, and $\beta(r)$ varies from $\beta(0) = 0$ to $\beta(R) = \pi/2$ for a Mermin-Ho coreless vortex [33] and from $\beta(0) = 0$ to $\beta(R) = \pi$ for an Anderson-Toulouse coreless vortex [34], where the outer edge of the condensate is at $r = R$ [21]. In Fig. 3(a), we plot the numerically obtained projection of the local magnetization vector on the xy plane for the axisymmetric $(0, +1, +2)$ vortex-bright soliton shown in Fig. 2(c) for parameters $c_0 = -4, c_1 = -0.25$, and $\gamma = 0.5$. The color of the arrows in Fig. 3(a), with value ranging from -1 to 1 , represents the z component of the local magnetization vector. Here the spin texture has been shown from origin to the second zero of ρ_0 which occurs at $r = 7.3$ in this case as in shown in Fig. 3(b). It is evident from Fig. 3(a) that the spin texture associated with axisymmetric $(0, +1, +2)$ vortex-bright soliton is consistent with the spin texture of an Anderson-Toulouse coreless vortex [21]. We find that from origin to the second zero of ρ_0 a $(0, +1, +2)$ vortex-bright soliton always has this spin texture. At the origin (the first zero of ρ_0), the spin points along positive z direction and it gets fully inverted at the second zero of ρ_0 . From the inset of Fig. 3(b), it is also evident that the densities of the three components actually have oscillations with multiple zeros. This oscillation and the consequent deviation from the Gaussian shape in density is the main reason for the difference in the analytic and variational density profiles shown in Fig. 2. Since the total norm ($2\pi \int r \rho(r) dr = 1$) for both the numerical and variational densities is the same, it implies that the

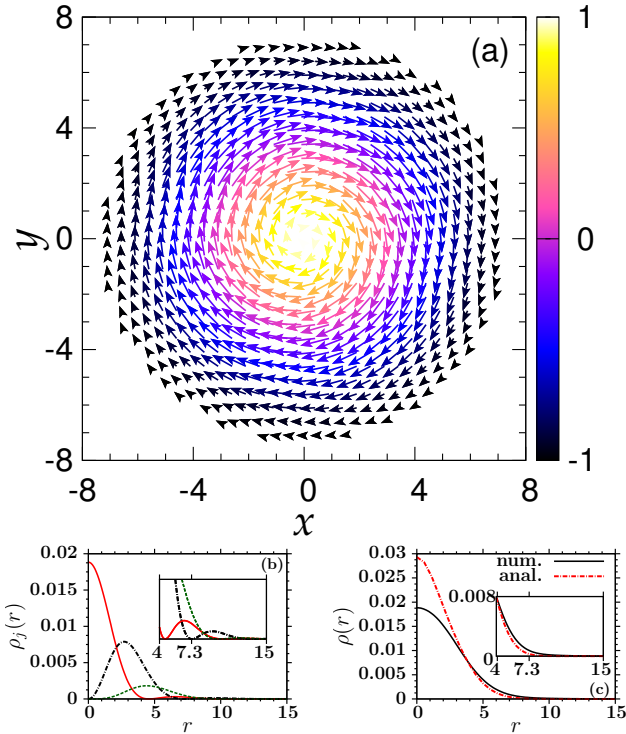


FIG. 3: (Color online) (a) The projection of local magnetization vector (normalized to unity) on the $x-y$ plane for the axisymmetric $(0, +1, +2)$ vortex-bright soliton of Fig. 2(c) with $c_0 = -4, c_1 = -0.25, \gamma = 0.5$. The color indicates the l_z component. At the center, color value of $+1$ indicates that the local magnetization vector is directed along $+z$ axis, similarly at the edge, color value of -1 indicated that the local magnetization vector is directed along $-z$ axis. (b) Numerical results for component densities $\rho_j(r)$ versus r for the axisymmetric $(0, +1, +2)$ vortex-bright soliton with $c_0 = -4, c_1 = -0.25, \gamma = 0.5$ showing the oscillation in density; here solid red, dot-dashed black and dashed green lines show the densities of $m_f = +1, m_f = 0$ and $m_f = -1$ components, respectively and the inset shows the zoom-in of main figure from $r = 4$ to $r = 15$. (c) Total numerical (num.) and variational or analytic (anal.) densities as a function of r for the axisymmetric $(0, +1, +2)$ vortex-bright soliton of Fig. 2(c); inset shows the same above the cross-over between the numerical and variational curves.

total variational density which is consistently larger than the numerical density near the origin, as can be inferred from Figs. 2(a)-(d), must be smaller than the total numerical density after a cross-over point. This is indeed the case for all the vortex-bright solitons shown in Fig. 2. To illustrate it for the vortex-bright soliton shown in Fig. 2(c), the total numerical and variational densities are shown in Fig. 3(c); the inset shows the densities in the domain where total numerical density is consistently higher than the variational one.

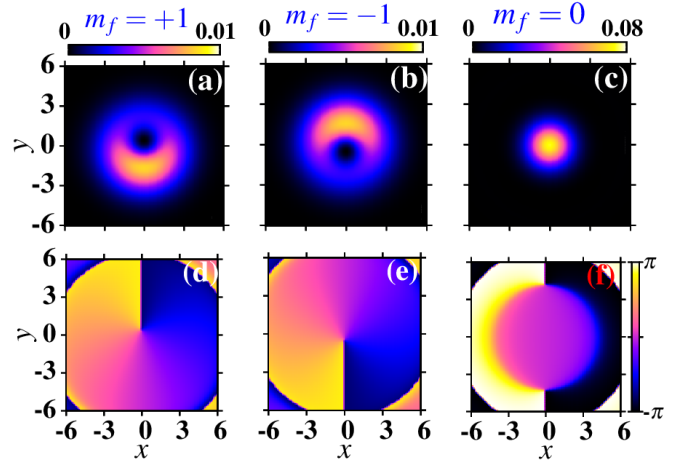


FIG. 4: (Color online) The 2D contour plot of densities of the components (a) $m_f = +1$, (b) $m_f = -1$, (c) $m_f = 0$ of an asymmetric soliton with $c_0 = -4, c_1 = -0.6$ and $\gamma = 0.5$. The corresponding phases are shown in (d) for $m_f = +1$, (e) for $m_f = -1$, and (f) for $m_f = 0$ components.

B. Asymmetric solitons

As c_1 is decreased further beyond $c_1^{(1)}$, e.g., for $c_1 < c_1^{(1)}$ the axisymmetric vortex-bright solitons cease to be the ground state and a new type of asymmetric soliton appears as the ground state. Nevertheless, the axisymmetric $(-1, 0, +1)$ and $(0, +1, +2)$ solitons are still dynamically stable vortex-soliton solutions, albeit with higher energy, for $c_1^{(2)} < c_1 < c_1^{(1)}$. The two-dimensional contour density and phase plots of the component wave functions for the numerically obtained minimum-energy asymmetric soliton with $c_0 = -4, c_1 = -0.6$ ($c_1 < c_1^{(1)}$) and $\gamma = 0.5$ are shown in Fig 4(a)-(f). The density corresponding to the component ψ_0 is axisymmetric, whereas the densities corresponding to components $\psi_{\pm 1}$ are *asymmetric*. However, the total density profile (not shown here) is still radially symmetric. The vortices in an asymmetric profile can lie along an arbitrary direction which will be spontaneously chosen in an experiment. This is due to the fact that Eqs. (3)-(4) and Eqs. (10)-(11) are invariant under simultaneous transformations: $\phi = \tan^{-1}(y/x) \rightarrow \phi + \theta$ and $\psi_{m_f}(r, \phi) \rightarrow \psi_{m_f}(r, \phi + \theta)e^{-im_f\theta}$, here θ is the angle of rotation. Keeping c_0 and γ fixed at -4 and 0.5 , respectively, if we decrease c_1 further from $c_1 = -0.6$, we find that the asymmetric ground-state soliton continues to exist for a sufficiently large negative c_1 ($-0.6 \geq c_1 \geq -1.8$) in this case, beyond which it collapses. As c_1 is decreased from -0.6 to -1.8 , the vortices in the components $\psi_{\pm 1}$ keep on moving away from each other, and finally can move out of the system. This can lead to a bright soliton with phase singularities lying at the edge of the condensate as is shown in Fig. 5 for $c_0 = -4, c_1 = -1.8$ and $\gamma = 0.5$. In figures Figs. 5(a)-(b) the solitons are bright solitons without any visible vortex core in density.

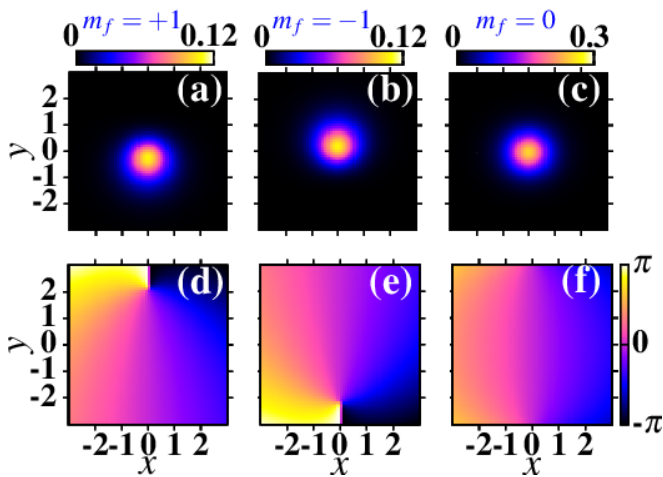


FIG. 5: (Color online) The 2D contour plot of densities of the components (a) $m_f = +1$, (b) $m_f = -1$, (c) $m_f = 0$ in an asymmetric soliton with $c_0 = -4$, $c_1 = -1.8$ and $\gamma = 0.5$. The corresponding phases are shown in (d) for $m_f = +1$, (e) for $m_f = -1$, and (f) for $m_f = 0$ components.

However, the phase jump corresponding to a vortex are seen in Figs. 5(d)-(e). It should be noted that as c_1 is decreased from -0.6 to -1.8 , the axisymmetric solitons shown in Figs. 2(a) and (c) are still stable vortex-solitons with energies higher than the asymmetric ground state.

The asymmetric solitons have non-zero contribution to energy from the c_1 dependent terms in contrast to the axisymmetric $(-1, 0, +1)$ vortex-bright soliton, and the details of the asymmetric soliton change as c_1 is changed as is illustrated by qualitative different bright solitons in Figs. 4 and 5. Similarly, the details of the axisymmetric $(0, +1, +2)$ vortex-bright soliton are also dependent on the value of c_1 .

C. Stability of solitons

Dynamical Stability: We find that an axisymmetric $(-1, 0, +1)$ vector soliton and an asymmetric soliton can emerge as the ground states depending upon the choice of interaction parameters c_0 , c_1 and γ . Both these solitons have zero magnetization and are dynamically stable. Similarly, the minimum energy axisymmetric $(0, +1, +2)$ vortex-bright soliton, which is an excited state and which has, in general, non-zero magnetization, is dynamically stable too.

To test the dynamical stability of the $(-1, 0, +1)$ vortex-bright solitons shown in Figs. 2(a) and (b) and the $(0, +1, +2)$ vortex-bright solitons shown in Figs. 2(c) and (d), we performed real-time simulation of the imaginary-time profiles as the initial state over a long interval of time. The steady oscillation of the root mean square (r_{rms}) sizes of the components as shown in Figs. 6 (a), (b), (c) and (d) corresponding, respectively, to solutions

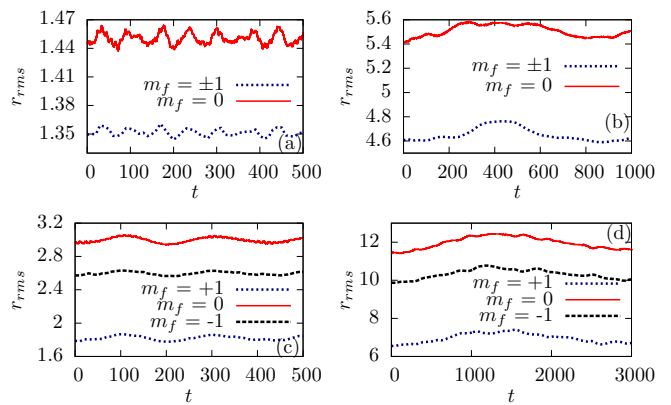


FIG. 6: (Color online) Numerical result of rms sizes of the component wave functions versus time as obtained in real-time simulation using the imaginary-time profiles of Figs. 2(a), (b), (c), and (d) as the initial states.

shown in Figs. 2 (a), (b), (c), and (d) demonstrates the stability of these solitons.

D. Stable moving solitons

In order to find the stable moving solitons, one needs to examine the Galilean invariance of the SO-coupled Hamiltonian. Using Galilean transformation $x' = x - vt$, $y' = y$, $t' = t$, where v is the relative velocity along x axis of the primed coordinate system with respect to unprimed coordinate system, and using the transformation

$$\psi_j(x, y, t) = \psi'_j(x', y', t')e^{ivx' + iv^2t'/2}, \quad (38)$$

in Eqs. (3)-(4), we get [17]

$$i\frac{\partial\psi'_{\pm 1}(\mathbf{r}')}{\partial t'} = \mathcal{H}\psi'_{\pm 1}(\mathbf{r}') \pm c_1 F'_z \psi'_{\pm 1}(\mathbf{r}') + \frac{c_1}{\sqrt{2}} F'_\mp \psi'_0(\mathbf{r}') - \frac{i\gamma}{\sqrt{2}} \left(\frac{\partial\psi'_0}{\partial x'} \mp i \frac{\partial\psi'_0}{\partial y'} \right) + \frac{\gamma}{\sqrt{2}} v \psi'_0, \quad (39)$$

$$i\frac{\partial\psi'_0(\mathbf{r}')}{\partial t'} = \mathcal{H}\psi'_0(\mathbf{r}') + \frac{c_1}{\sqrt{2}} [F'_- \psi'_{-1}(\mathbf{r}') + F'_+ \psi'_{+1}(\mathbf{r}')] - \frac{i\gamma}{\sqrt{2}} \left(\frac{\partial\psi'_1}{\partial x} + i \frac{\partial\psi'_1}{\partial y'} + \frac{\partial\psi'_{-1}}{\partial x'} - i \frac{\partial\psi'_{-1}}{\partial y'} \right) + \frac{\gamma}{\sqrt{2}} v (\psi'_{+1} + \psi'_{-1}). \quad (40)$$

Due to v dependent terms in Eqs. (39)-(40), the system is not Galilean invariant. Here for the sake of simplicity, we have considered motion along x axis. In the absence of SO coupling ($\gamma = 0$), the Galilean invariance is restored, implying that the moving solitons, given by Eq. (38), can be trivially obtained by multiplying stationary solutions of Eqs. (3)-(4) with e^{ivx} . This is no longer possible for $\gamma \neq 0$, in which case, the moving solitons

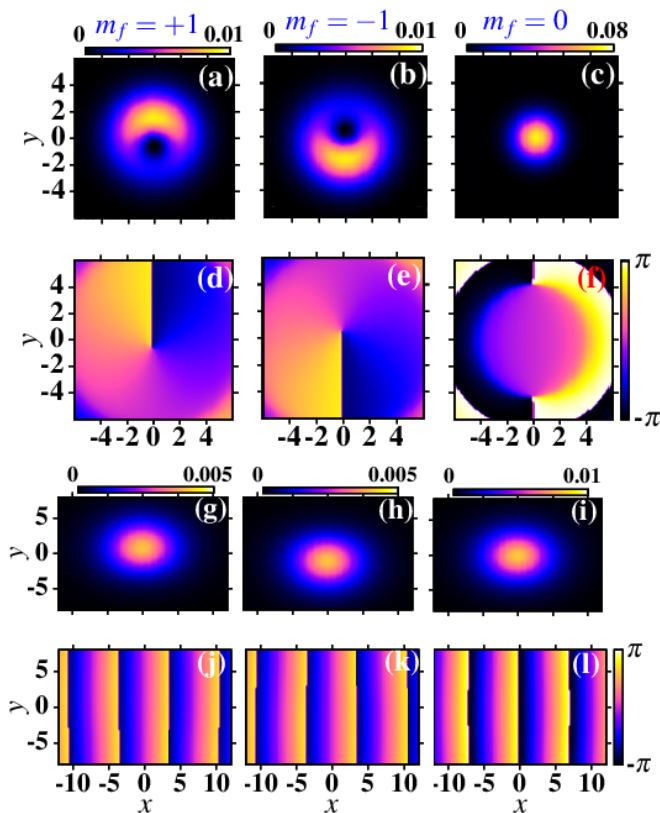


FIG. 7: (Color online) The 2D contour plot of the (a) density of component $m_f = +1$, (b) density of component $m_f = -1$, (c) density of component $m_f = 0$, of the dynamically stable asymmetric soliton moving with a speed of 0.01 along the x axis for $c_0 = -4, c_1 = -0.25, \gamma = 0.5$; the respective phases are shown in (d)-(f). In (a) and (b) the holes in the density profiles are antivortex and vortex, respectively. The density and phase of the components $m_f = +1, -1$ and 0 of the dynamically stable soliton with the same parameters moving with a speed of 0.4 along x axis are shown in (g)-(i) and (j)-(l), respectively.

are the stationary solutions, presuming that these exist, of Eqs. (39)-(40) multiplied by e^{ivx} [13, 15, 16]. The dependence of the shape of the soliton on its velocity is illustrated in Fig. 7, where we present the 2D contour plot of the density and phase of a soliton moving from left to right along x axis with velocity $v = 0.01$ and 0.4 for the parameters $c_0 = -4, c_1 = -0.25$, and $\gamma = 0.5$. The density and phase for $v = 0.01$ in Figs. 7(a)-(f) clearly show the vortex and antivortex in components $m_f = \pm 1$, whereas in Figs. 7(g)-(l) we find that the vortex and antivortex have disappeared. These solutions, viz. $\psi_j(x, y, 0)$ in Eq. (38), obtained by solving Eqs. (39)-(40) in imaginary-time simulation and then multiplied by e^{ivx} are dynamically stable as confirmed in real-time simulation of these solutions using Eqs. (3)-(4). The moving soliton has an asymmetric profile, whereas the stationary soliton for the same set of parameters shown

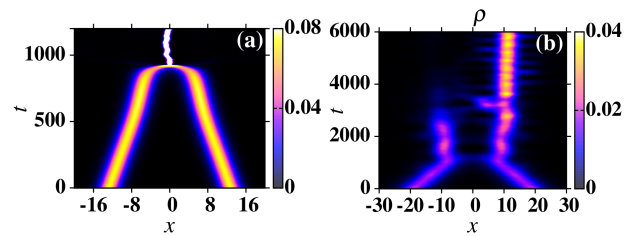


FIG. 8: (Color online) (a) The 2D contour plot of the total density $\rho(x, y = 0, t)$ versus x and t during the collision of two *in-phase* vortex-bright solitons, each with $c_0 = -4, c_1 = -0.25$ and $\gamma = 0.5$, moving in opposite directions along x axis with velocity $v = 0.01$. (b) shows the same for $c_0 = -2, c_1 = -0.25$ and $\gamma = 0.5$.

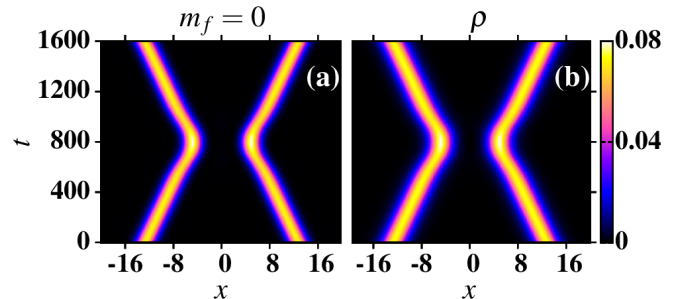


FIG. 9: (Color online) The 2D contour plot of (a) the density of the $m_f = 0$ component $\rho_0(x, y = 0, t)$ and (b) total density $\rho(x, y = 0, t)$ versus x and t during the collision of two *out-of-phase* solitons considered in Fig. (7) moving in opposite directions each with a speed $v = 0.01$. The absence of crossing of the tracks in (a) and (b) illustrates that the solitons rebound after the encounter.

in Fig. 2(a) is axisymmetric. However, the density of the $m_f = 0$ component of the moving vortex-bright soliton shown in Figs. 7 is axisymmetric; the same is true about the total density. The result shown in Figs. 7 is a manifestation of the lack of Galilean invariance in the present system which makes the density profile of the moving soliton a function of its velocity – both magnitude and direction. Keeping $c_0 = -4, c_1 = -0.25$ and $\gamma = 0.5$ fixed, we find that the Eqs. (39)-(40) allow the self-trapped stationary solutions for $v \leq 0.4$ along the x axis; for $v > 0.4$ along the x axis, no localized solitons can be found. As we increase v from zero, the vortices in components $m_f = +1$ and $m_f = -1$ start moving away from each other along y axis. Numerically, we also find that these vortices are located on the line perpendicular to the direction of motion. The Eqs. (39)-(40) are no longer invariant under transformations: $\phi = \tan^{-1}(y/x) \rightarrow \phi + \theta$ and $\psi_{m_f}(r, \phi) \rightarrow \psi_{m_f}(r, \phi + \theta)e^{-im_f\theta}$ due to v dependent terms. The orientation of the vortices in the stationary solutions of Eqs. (39)-(40) along y axis is the manifestation of the lack of this rotational symmetry.

The collision between two one-dimensional integrable

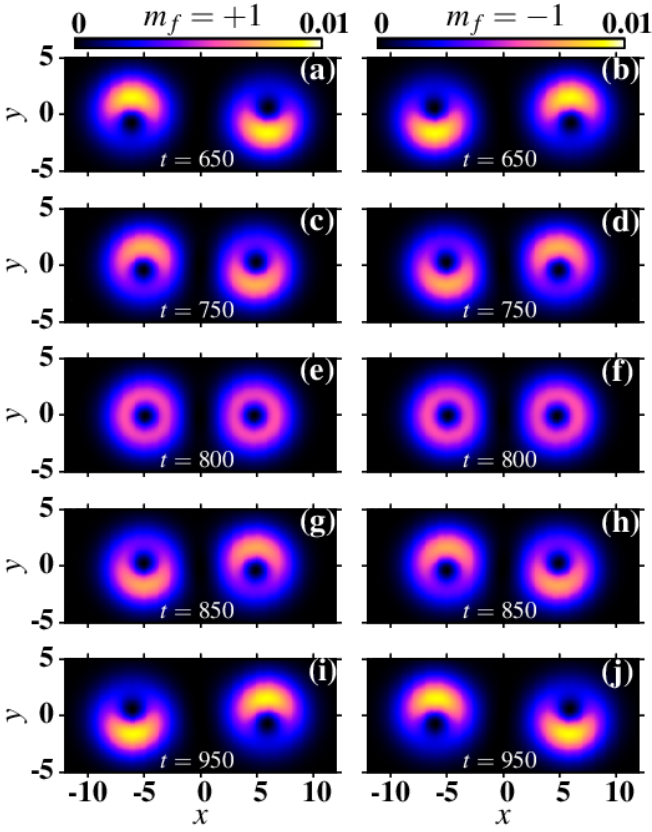


FIG. 10: (Color online) The 2D contour plot of densities of the $m_f = +1$ component in the right and left moving solitons during collision shown in Fig. 9 at times (a) $t = 650$, (c) $t = 750$, (e) $t = 800$, (g) $t = 850$, and (i) $t = 950$. The same for the densities of the $m_f = -1$ component in the right and left moving soliton are shown in (b) $t = 650$, (d) $t = 750$, (f) $t = 800$, (h) $t = 850$, and (j) $t = 950$. At $t = 800$ the distance between the two colliding solitons is minimum. Holes in the density profiles of the $m_f = +1$ component correspond to antivortices, whereas the holes in density profiles of the $m_f = -1$ component correspond to vortices.

solitons is truly elastic. The collision between two 2D solitons is expected to be inelastic, in general. We find that the two *in-phase* vortex-bright solitons for $c_0 = -4$, $c_1 = -0.25$, $\gamma = 0.5$ and moving with speed of $v = 0.01$ in opposite directions collapse after collision as is shown Fig. 8(a). In order to avert collapse, we considered the collision between the *in-phase* vortex-bright solitons with $c_0 = -2$ (half of the previous value), $c_1 = -0.25$, $\gamma = 0.5$, and $v = 0.01$. In this case after the collision, all the atoms are transferred to one of the solitons as is shown in Fig. 8(b) and hence, effectively leads to merger as has also been observed experimentally for scalar solitons [25]. The collision in this case has similarity to the inelastic collision between the two non-spinor bright solitons at low velocities [24]. However, we find that the slowly moving $(-1, 0, +1)$ solitons with asymmetric profiles, like the ones shown in Fig. 7, and a phase difference of π can

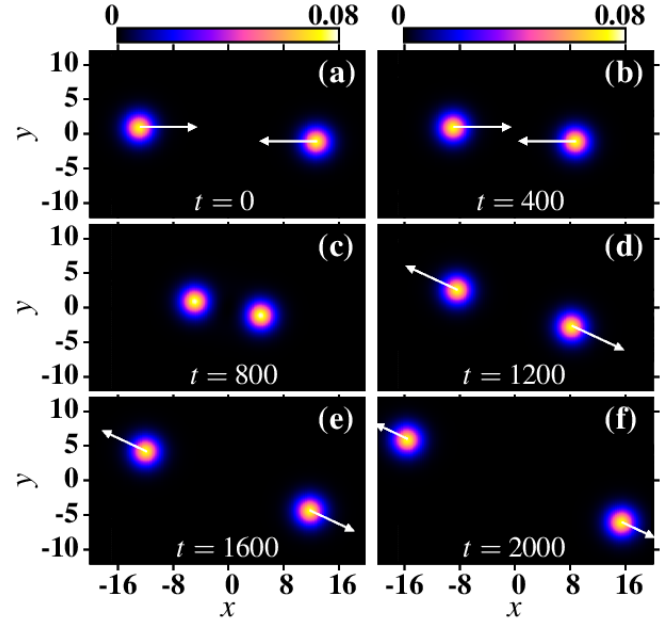


FIG. 11: (Color online) The 2D contour plot of total densities of the right and left moving *out-of-phase* solitons with the same parameters as in Fig. 7 during collision with the impact parameter $d = 2$, each moving with a speed $v = 0.01$, at times (a) $t = 0$, (b) $t = 400$, (c) $t = 800$, (d) $t = 1200$, (e) $t = 1600$, and (f) $t = 2000$. The direction of motion of the solitons before and after collision are indicated by white arrows in (a) and (d), respectively, illustrating a change in the direction of motion after collision. In this case the solitons repel and avoid each other without a direct encounter.

collide quasi-elastically. This is demonstrated by real-time simulation of two solitons, obtained by solving Eqs. (39)-(40) for $c_0 = -4$, $c_1 = -0.25$, $\gamma = 0.5$ and $v = 0.01$ by imaginary-time propagation, placed initially at $t = 0$ at $x = \pm 12.7$ and set into motion in opposite directions along x axis with a speed of $v = 0.01$. In our simulations, if we use the same initial guess to obtain the right and left moving solitons, they end up acquiring a phase difference of π . We find that the solitons come close to each other and turn back and retrace their trajectory without crossing each other. This is illustrated by the 2D contour plot of the axisymmetric $m_f = 0$ component and total densities, (a) $\rho_0(x, y = 0, t)$ and (b) $\rho(x, y = 0, t)$, respectively, versus x and t in Fig. 9. During the collision, the asymmetric densities of $m_f = \pm 1$ components show subtle changes as are shown in Fig. 10 through snapshots of subsequent 2D contour plots of these densities near the instant of closest approach of the two solitons. The density distribution of $m_f = \pm 1$ components in the right and the left moving solitons are not identical as is shown in Figs. 10(a) and (b), which is again due to the break-down of the Galilean invariance. As the left and the right moving solitons collide, the antivortices in the $m_f = +1$ component in the left and the right moving solitons slowly move along the y axis as is evident from

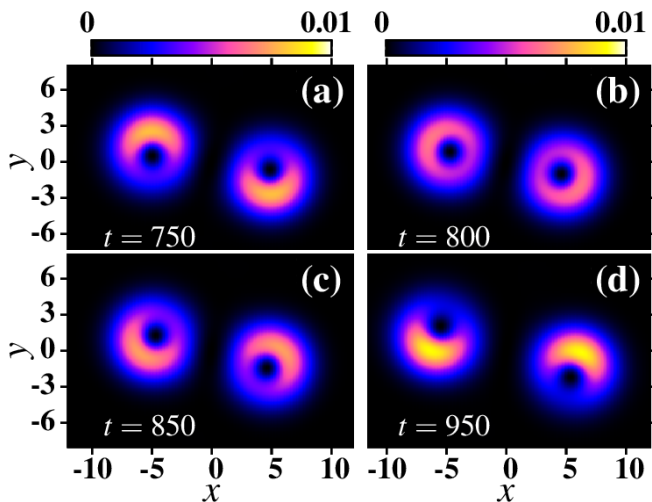


FIG. 12: (Color online) Dynamics of the antivortex cores, close to the positions of closest approach, of $m_f = +1$ components in the right and left moving solitons for the collision shown in Fig. 11. The holes in the density profiles are the antivortices.

Figs. 10 (a), (c), (e), (g), and (i); this is accompanied by an analogous movement of vortices in ψ_{-1} as is shown in Figs. 10 (b), (d), (f), (h), and (j). These changes ensure that during the course of the collision the two solitons exchange their linear momenta, and thus rebound after collision without ever crossing each other. The repulsive collision between the two bright solitons in a quasi-1D BEC has also been observed experimentally [25] consistent with our simulations.

We have also investigated the *out-of-phase* collision between two slowly moving solitons along x axis in opposite directions with non-zero impact parameter d . We consider elastic collision between two bright solitons, each with $c_0 = -4$, $c_1 = -0.25$ and $\gamma = 0.5$, placed initially ($t = 0$) at $x = \pm 12.7, y = \pm 1$ and set into motion along the x axis in opposite directions with speed $v = 0.01$. This collision is illustrated in Fig. 11 by the 2D contour plot of the total densities of the two colliding solitons. As in an elastic collision with non-zero impact parameter between two classical objects, the two solitons are deflected from their original trajectory conserving momentum; they do not retrace their trajectories after collision as in Fig. 9. The direction of motion of the solitons before and after collision are shown by white arrows in Figs. 11(a) and (d), respectively. As in the case of head-on collision shown in Fig. 10, here too the vortices in left and right moving solitons rearrange themselves consistent with the change in the direction of motion during the collision. The change in the density profile of the $m_f = +1$ component during the collision is shown in Fig. 12; this is accompanied by an analogous change in the density profile of the $m_f = -1$ component (not shown here), viz. Fig. 10.

The *out-of-phase* collision illustrated in Figs. 11 can be

TABLE I: Numerical and analytical result for the angles of the emerging solitons after collision shown in Fig. 11.

d	numerical		analytical	
	θ'_1	θ'_2	θ'_1	θ'_2
1	168.5	348.5	167.8	347.8
2	155.2	335.2	155.4	335.4
3	142.2	322.2	142.8	322.8
4	130.2	310.2	129.6	309.6

theoretically analyzed by considering the collision to be equivalent to classical elastic collision between two identical rigid circular disks of equal mass and equal scalar velocity v with a non-zero impact parameter d . If the initial velocities of the two disks are

$$\mathbf{v}_j = v \cos \theta_j \hat{x} + v \sin \theta_j \hat{y}, \quad (41)$$

where $j = 1, 2$ denote the index of the disk, \hat{x} and \hat{y} are the unit vectors along x and y axes, respectively; then the velocity components, (v'_{jx}, v'_{jy}) , after collision are [35]

$$v'_{jx} = v \cos(\theta_{3-j} - \phi) \cos \phi - v \sin(\theta_j - \phi) \sin \phi, \quad (42)$$

$$v'_{jy} = v \cos(\theta_{3-j} - \phi) \sin \phi + v \sin(\theta_j - \phi) \cos \phi. \quad (43)$$

Here ϕ is the collision angle and is related to the coordinates of the centers of two disks at the instant of closest approach, denoted by (C_{jx}, C_{jy}) , as

$$\phi = \tan^{-1} \left(\frac{C_{1y} - C_{2y}}{C_{1x} - C_{2x}} \right). \quad (44)$$

In our case, when the two solitons are moving along $y = +d/2$, $\theta_1 = 0$ and $y = -d/2$ and $\theta_2 = \pi$, ϕ can be written in terms of the impenetrable radius R of the soliton

$$\phi = -\tan^{-1} \left(\frac{d}{\sqrt{4R^2 - d^2}} \right), \quad (45)$$

where impenetrable radius can be defined as the half of the distance between the centers of the two solitons at the distance of closest approach and is equal to 4.7 in the present case. Besides the collision shown in Fig. 11 with impact parameter $d = 2$, we also studied the collisions with $d = 1, 3, 4$. Using $\theta_1 = 0$, $\theta_2 = \pi$ in Eqs. (42)-(43), we find that the magnitude of the velocities of the solitons remain unchanged after collision which is consistent with numerical findings. The final angles are given by $\theta'_1 = \pi + 2\phi$ and $\theta'_2 = 2\pi + 2\phi$. These analytic classical results for the elastic collision between two disks are in good agreement with the numerical result of elastic collision between two quantum 2D BEC solitons for $v_1 = v_2 = 0.01$, $\theta_1 = 0$, $\theta_2 = \pi$ and $R = 4.7$. The numerical and analytic results for θ'_j 's in *degrees* for different values of impact parameters are summarized in Table I.

In contrast to slowly moving vortex-bright solitons, two fast moving vortex solitons can pass through each

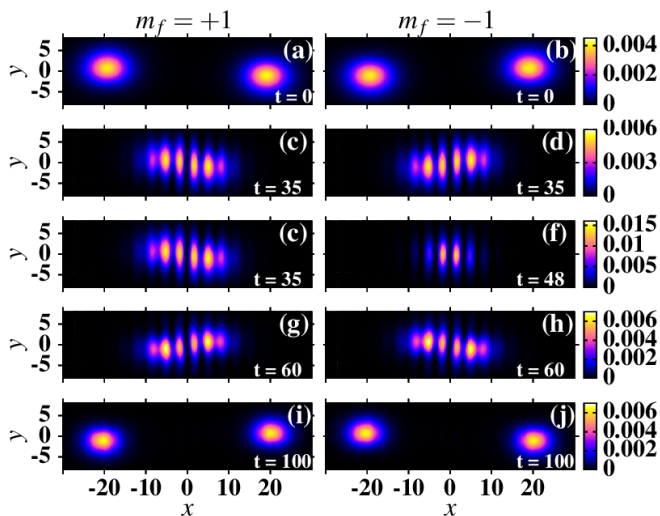


FIG. 13: (Color online) The 2D contour plot of densities of the $m_f = +1$ components of two *in-phase* vortex-bright solitons each with $c_0 = -4$, $c_1 = -0.25$ and $\gamma = 0.5$ moving in opposite directions along x axis with velocity $v = 0.4$ at times $t =$ (a) 0, (c) 35, (e) 48, (g) 60, and (i) 100. The same for the $m_f = -1$ components are, respectively, presented in (b), (d), (f), (h), and (j).

other during collision irrespective of phase difference. To demonstrate this, we consider the head-on collision between two *in-phase* vortex-bright solitons, each with $c_0 = -4$, $c_1 = -0.25$ and $\gamma = 0.5$, moving with a speed of 0.4 in opposite directions along the x axis. The collision is illustrated by successive snapshots of 2D contour plots of $m_f = \pm 1$ components in Figs. 13. In this case, the collision dynamics of two *out-of-phase* vortex-bright solitons with same c_0, c_1, γ and v has little difference from dynamics shown in Figs. 13. This figure is qualitatively different from the dynamics shown in Fig. 8(b) where at low velocities the solitons do not pass through each other. However, Figs. 13 reveal that at high velocities the solitons superpose and cross each other like normal BEC solitons in 1D [36] and 2D [37].

V. SUMMARY

We have studied the formation and dynamics of 2D vortex-bright solitons in a three-component SO-coupled spin-1 spinor condensate using numerical solution and variational approximation of the mean-field GP equation. The ground state vortex-bright solitons are axisymmetric in the 2D plane in the polar ($c_1 > 0$) and weakly ferromagnetic ($0 > c_1 > c_1^{(1)}$) domains, whereas they are asymmetric in the strongly ferromagnetic domain ($c_1^{(1)} > c_1 > c_1^{(2)}$). For very strong ferromagnetic interaction ($c_1 < c_1^{(2)}$) the system collapsed and no solitons can be found. In this problem the coupled GP equations are not Galilean invariant. Consequently, to obtain the dynamically stable moving solitons, the Galilean-transformed coupled GP equations have been used. The profile of the moving soliton is dependent on its velocity vector. In the study of collision of two moving vortex-bright solitons at small velocities, we find that the *in-phase* solitons either collapse or merge into single entity, whereas *out-of-phase* solitons repel and avoid each other without ever having an overlapping profile. The collision between the *in-phase* vortex-bright solitons is thus qualitatively similar to the collision of two normal (non-spinor) BEC solitons in 1D [36] and 2D [37]. In the collision of two solitons at large velocities, they form an overlapping profile during interaction and cross each other. Here, the phase difference between the two solitons has little effect on the collision dynamics as the kinetic energy of the solitons is more than sufficient to overcome any repulsion arising due to the phase difference.

Acknowledgments

This work is financed by the Fundação de Amparo à Pesquisa do Estado de São Paulo (Brazil) under Contract Nos. 2013/07213-0, 2012/00451-0 and also by the Conselho Nacional de Desenvolvimento Científico e Tecnológico (Brazil).

-
- [1] Y. S. Kivshar and B. A. Malomed, Rev. Mod. Phys. **61**, 763 (1989); F. K. Abdullaev, A. Gammal, A. M. Kamchatnov, and L. Tomio, Int. J. Mod. Phys. B **19**, 3415 (2005).
- [2] S. Inouye, M. R. Andrews, J. Stenger, H.-J. Miesner, D. M. Stamper-Kurn, and W. Ketterle, Nature (London) **392**, 151 (1998).
- [3] K. E. Strecker, G. B. Partridge, A. G. Truscott, and R. G. Hulet, Nature (London) **417**, 150 (2002); L. Khaykovich, F. Schreck, G. Ferrari, T. Bourdel, J. Cubizolles, L. D. Carr, Y. Castin, and C. Salomon, Science **256**, 1290 (2002).
- [4] S. L. Cornish, S. T. Thompson, and C. E. Wieman, Phys. Rev. Lett. **96**, 170401 (2006).
- [5] V. M. Pérez-García and J. B. Beitia, Phys. Rev. A **72**, 033620 (2005); S. K. Adhikari, Phys. Lett. A **346**, 179 (2005); Phys. Rev. A **72**, 053608 (2005); L. Salasnich and B. A. Malomed, Phys. Rev. A **74**, 053610 (2006).
- [6] J. Ieda, T. Miyakawa, and M. Wadati, Phys. Rev. Lett. **93**, 194102 (2004); L. Li, Z. Li, B. A. Malomed, D. Mihalache, and W. M. Liu, Phys. Rev. A **72**, 033611 (2005); W. Zhang, Ö. E. Müstecaplıoğlu, and L. You, Phys. Rev. A **75**, 043601 (2007); B. J. Dąbrowska-Wüster, E. A. Ostrovskaya, T. J. Alexander, and Y. S. Kivshar, Phys. Rev. A **75**, 023617 (2007); E. V. Doktorov, J. Wang, and J. Yang, Phys. Rev. A **77**, 043617 (2008); B. Xiong and J.

- Gong; Phys. Rev. A **81**, 033618 (2010); P. Szankowski, M. Trippenbach, E. Infeld, and G. Rowlands, Phys. Rev. Lett. **105**, 125302 (2010).
- [7] Y. Li, Giovanni I. Martone, and S. Stringari, *Annual Review of Cold Atoms and Molecules*, Vol. 3, (World Scientific, 2015), 201-250; V. Galitski and I. B. Spielman, Nature **494**, 49 (2013).
- [8] K. Osterloh, M. Baig, L. Santos, P. Zoller, and M. Lewenstein, Phys. Rev. Lett. **95**, 010403 (2005); J. Ruseckas, G. Juzeliūnas, P. Öhberg, and M. Fleischhauer, Phys. Rev. Lett. **95**, 010404 (2005); G. Juzeliūnas, J. Ruseckas, and J. Dalibard, Phys. Rev. A **81**, 053403 (2010); Z. Lan and P. Öhberg, Rev. Mod. Phys. **83**, 1523 (2011).
- [9] Y. A. Bychkov E. I. Rashba, J. Phys. C **17**, 6039 (1984).
- [10] G. Dresselhaus, Phys. Rev. **100**, 580 (1955).
- [11] Y.-J. Lin, K. Jiménez-García, and I. B. Spielman, Nature **471**, 83 (2011).
- [12] M. Aidelsburger, M. Atala, and S. Nascimbéne, S. Trotzky, Y.-A. Chen, and I. Bloch, Phys. Rev. Lett. **107**, 255301 (2011); Z. Fu, P. Wang, and S. Chai, L. Huang, and J. Zhang, Phys. Rev. A **84**, 043609 (2011); J.-Y. Zhang, S.-C. Ji, Z. Chen, L. Zhang, Z.-D. Du, B. Yan, G.-S. Pan, B. Zhao, Y.-J. Deng, H. Zhai, S. Chen, and J.-W. Pan, Phys. Rev. Lett. **109**, 115301 (2012); C. Qu, C. Hammer, M. Gong, C. Zhang, and P. Engels, Phys. Rev. A **88**, 021604(R) (2013).
- [13] Y. Xu, Y. Zhang, and B. Wu, Phys. Rev. A **87**, 013614 (2013).
- [14] L. Salasnich and B. A. Malomed, Phys. Rev. A **87**, 063625 (2013); L. Salasnich, W. B. Cardoso, and B. A. Malomed, Phys. Rev. A **90**, 033629 (2014); S. Cao, C.-J. Shan, D.-W. Zhang, X. Qin, and J. Xu, J. Opt. Soc. Am. B **32**, 201 (2015).
- [15] H. Sakaguchi, B. Li, and B. A. Malomed, Phys. Rev. E **89**, 032920 (2014); H. Sakaguchi and B. A. Malomed, Phys. Rev. E **90**, 062922 (2014).
- [16] Y.-K. Liu and S.-J. Yang, Eur. Phys. Lett., **108**, 30004 (2014).
- [17] S. Gautam and S. K. Adhikari, Laser Phys. Lett. **12**, 045501 (2015).
- [18] S. Gautam and S. K. Adhikari, Phys. Rev. A **91**, 063617 (2015).
- [19] L. Salasnich, A. Parola, and L. Reatto, Phys. Rev. A **65**, 043614 (2002).
- [20] T. Ohmi, and K. Machida, J. Phys. Soc. Japan, **67**, 1822 (1998); T. L. Ho, Phys. Rev. Lett. **81**, 742 (1998).
- [21] T. Mizushima, K. Machida, and T. Kita, Phys. Rev. Lett. **89**, 030401 (2002); Phys. Rev. A **66**, 053610 (2002).
- [22] S. Gautam and S. K. Adhikari, Phys. Rev. A **93**, 013630 (2016); Phys. Rev. A **92**, 023616 (2015); Phys. Rev. A **91**, 013624 (2015); Phys. Rev. A **90**, 043619 (2014).
- [23] D. L. Campbell, R. M. Price, A. Putra, A. ValdÁs-Curiel, D. Trypogeorgos, and I. B. Spielman, Nature Commun. **7**, 10897 (2016).
- [24] Luis E. Young-S, P. Muruganandam, and S. K. Adhikari, J. Phys. B **44**, 101001 (2011).
- [25] J. H. V. Nguyen, P. Dyke, D. Luo, B. A. Malomed, and R. G. Hulet, Nature Physics **10**, 918 (2014).
- [26] H. Zhai, Int. J. of Mod. Phys. B, **26**, 1230001 (2012).
- [27] Y. Kawaguchi and M. Ueda, Phys. Rep. **520**, 253 (2012).
- [28] P. Muruganandam and S. K. Adhikari, J. Phys. B **36**, 2501 (2003).
- [29] H. Wang, J. Comput. Phys., **230**, 6155 (2011); **274**, 473 (2014).
- [30] W. Bao and F. Y. Lim, Siam J. Sci. Comp. **30**, 1925 (2008); F. Y. Lim and W. Bao, Phys. Rev. E **78**, 066704 (2008).
- [31] P. Muruganandam and S. K. Adhikari, Comput. Phys. Commun. **180**, 1888 (2009); D. Vudragović, I. Vidanović, A. Balaž, P. Muruganandam, and S. K. Adhikari, Comput. Phys. Commun. **183**, 2021 (2012); L. E. Young-S., D. Vudragovic, P. Muruganandam, S. K. Adhikari, and A. Balaž, Comput. Phys. Commun. **204**, 209 (2016); B. Satarić, V. Slavnić, A. Belić, A. Balaž, P. Muruganandam, and S. K. Adhikari, Comput. Phys. Commun. **200**, 411 (2016); R. Kishor Kumar, L. E. Young-S., D. Vudragović, Antun Balaž, P. Muruganandam, S. K. Adhikari, Comput. Phys. Commun. **195**, 117 (2015).
- [32] J.-P. Martikainen, *Dynamics and excitations of Bose-Einstein condensates*, Academic dissertation, Helsinki Institute of Physics, University of Helsinki (2001).
- [33] N. D. Mermin and Tin-Lun Ho, Phys. Rev. Lett. **36**, 594 (1976).
- [34] P.W. Anderson and G. Toulouse, Phys. Rev. Lett. **38**, 508 (1977).
- [35] Robert A. Becker, *Introduction to Theoretical Mechanics*, McGraw-Hill Book Company, 1954.
- [36] S. K. Adhikari, New J. Phys **5**, 137 (2003).
- [37] P. Pedri and L. Santos, Phys. Rev. Lett. **95**, 200404 (2005); S. K. Adhikari, J. Phys. B **47**, 225304 (2014).